CO_2 surface fluxes at grid point scale estimated from a global 21 year reanalysis of atmospheric measurements

F. Chevallier,[1] P. Ciais,[1] T. J. Conway,[2] T. Aalto,[3] B. E. Anderson,[4] P. Bousquet,[1] E. G. Brunke,[5] L. Ciattaglia,[6] Y. Esaki,[7] M. Fröhlich,[8] A. Gomez,[9] A. J. Gomez-Pelaez,[10] L. Haszpra,[11] P. B. Krummel,[12] R. L. Langenfelds,[12] M. Leuenberger,[13] T. Machida,[14] F. Maignan,[1] H. Matsueda,[15] J. A. Morguí,[16] H. Mukai,[14] T. Nakazawa,[17] P. Peylin,[1] M. Ramonet,[1] L. Rivier,[1] Y. Sawa,[15] M. Schmidt,[1] L. P. Steele,[12] S. A. Vay,[4] A. T. Vermeulen,[18] S. Wofsy,[19] and D. Worthy[20]

Received 18 January 2010; revised 1 June 2010; accepted 2 July 2010; published 9 November 2010.

[1] This paper documents a global Bayesian variational inversion of CO_2 surface fluxes during the period 1988–2008. Weekly fluxes are estimated on a 3.75° × 2.5° (longitude-latitude) grid throughout the 21 years. The assimilated observations include 128 station records from three large data sets of surface CO_2 mixing ratio measurements. A Monte Carlo approach rigorously quantifies the theoretical uncertainty of the inverted fluxes at various space and time scales, which is particularly important for proper interpretation of the inverted fluxes. Fluxes are evaluated indirectly against two independent CO_2 vertical profile data sets constructed from aircraft measurements in the boundary layer and in the free troposphere. The skill of the inversion is evaluated by the improvement brought over a simple benchmark flux estimation based on the observed atmospheric growth rate. Our error analysis indicates that the carbon budget from the inversion should be more accurate than the a priori carbon budget by 20% to 60% for terrestrial fluxes aggregated at the scale of subcontinental regions in the Northern Hemisphere and over a year, but the inversion cannot clearly distinguish between the regional carbon budgets within a continent. On the basis of the independent observations, the inversion is seen to improve the fluxes compared to the benchmark: the atmospheric simulation of CO_2 with the Bayesian inversion method is better by about 1 ppm than the benchmark in the free troposphere, despite possible systematic transport errors. The inversion achieves this improvement by changing the regional fluxes over land at the seasonal and at the interannual time scales.

Citation: Chevallier, F., et al. (2010), CO_2 surface fluxes at grid point scale estimated from a global 21 year reanalysis of atmospheric measurements, *J. Geophys. Res.*, *115*, D21307, doi:10.1029/2010JD013887.

1. Introduction

[2] Carbon atoms have the exceptional ability to form stable chemical bonds with each other and therefore participate in all living organisms on Earth. Their ubiquity, the ability of living organisms to reduce carbon dioxide and to oxidize carbon to carbon dioxide through photosynthesis and respiration and the carbonate-chemistry system in water, translates into diverse individual processes that contribute to the carbon balance at the Earth-atmosphere interface. With the growing contribution of human activities in the carbon cycle, the quantification of this carbon balance at regional

[1]Laboratoire des Sciences du Climat et de l'Environnement, CEA-CNRS-UVSQ, IPSL, Gif-sur-Yvette, France.
[2]Earth System Research Laboratory, NOAA, Boulder, Colorado, USA.
[3]Finnish Meteorological Institute, Helsinki, Finland.
[4]Langley Research Center, NASA, Hampton, Virginia, USA.
[5]South African Weather Service, Stellenbosch, South Africa.
[6]ICES CNR-IDAC, Rome, Italy.
[7]Japan Meteorological Agency, Tokyo, Japan.
[8]Umweltbundesamt GmbH, Vienna, Austria.
[9]National Institute for Water and Atmospheric Research, Wellington, New Zealand.
[10]Meteorological State Agency of Spain, Santa Cruz de Tenerife, Spain.
[11]Hungarian Meteorological Service, Budapest, Hungary.
[12]Centre for Australian Weather and Climate Research/CSIRO Marine and Atmospheric Research, Aspendale, Victoria, Australia.
[13]Climate and Environmental Physics, Physics Institute, and Oeschger Center for Climate Change Research, University of Bern, Bern, Switzerland.
[14]National Institute for Environmental Studies, Tsukuba, Japan.
[15]Meteorological Research Institute, Tsukuba, Japan.
[16]Laboratori de Recerca del Clima, Barcelona, Spain.
[17]Tohoku University, Sendai, Japan.
[18]Energy Research Centre of the Netherlands, Petten, Netherlands.
[19]School of Engineering and Applied Sciences, Harvard University, Cambridge, Massachusetts, USA.
[20]Environment Canada, Downsview, Ontario, Canada.

0148-0227/10/2010JD013887

scales has become a major scientific challenge that is being tackled by experimentalists and modelers. At present, direct carbon flux measurements lack the spatial coverage needed to map the fluxes accurately. Numerical models of the carbon cycle, informed by process studies and specific inventories, lack the sophistication to pin down the variability of the carbon surface sources and sinks. In this context, atmospheric CO_2 mixing ratio measurements form a complementary source of information about the fluxes, because atmospheric mixing integrates the individual contributions from the fluxes at large spatial and temporal scales. However, the transformation of the CO_2 mixing ratio gradients into carbon fluxes involves sophisticated statistical inversion schemes and atmospheric transport models that are still a topic of active research [e.g., *Rödenbeck et al.*, 2003; *Peters et al.*, 2007].

[3] This paper reports on a collective effort to analyze the CO_2 surface fluxes over two decades, from 1988 to 2008, based on CO_2 mixing ratio records from three large databases: the NOAA Earth System Research Laboratory (ESRL) archive, the CarboEurope IP project, and the World Data Centre for Greenhouse Gases (WDCGG) of the World Meteorological Organization (WMO) Global Atmosphere Watch Programme. The three databases include both in situ measurements made by automated quasicontinuous analyzers and air samples collected in flasks and later analyzed at central facilities. The flux inversion builds on the variational Bayesian inversion system of *Chevallier et al.* [2005], which allows the fluxes to be estimated at a relatively high resolution over the globe: 8 days and 3.75° × 2.5° (longitude-latitude). The period of analysis covers 21 years, from 1988 to 2008. Fluxes and mixing ratios are linked in the system by the global atmospheric transport model of the Laboratoire de Météorologie Dynamique (LMDZ [*Hourdin et al.*, 2006]). A series of flux inventories, flux climatologies, flux models, and flux error models regularizes the solution to the flux inference problem. The uncertainty of the inverted fluxes is quantified from the Bayesian theory by the Monte Carlo method of *Chevallier et al*. [2007]. Independent validation data are provided by 34 aircraft measurement campaigns gathered in the GEOMON database (http://geomon-wg.ipsl.jussieu.fr/sections/aircraftcampaigns) and by the commercial-aircraft-based observations in the Comprehensive Observation Network for Trace gases by Airliner (CONTRAIL) database [*Machida et al.*, 2008]. As a benchmark to evaluate the quality of the fluxes resulting from our inversion, we use a simpler inversion called the "poor man's inversion," based only on the global annual CO_2 growth rate information.

[4] The paper is structured as follows. Section 2 describes the inversion method. The validation strategy is described in section 3. The results are presented in section 4. Section 5 concludes the paper.

2. Inversion Method

2.1. Inversion System

[5] The variations of CO_2 surface fluxes over the 21 year period (1988–2008) are inferred from the atmospheric measurements by the inversion scheme of *Chevallier et al*. [2005], which combines them with a global transport model and some preexisting information about the fluxes within a Bayesian framework. Following the usual terminology, "prior" designates the flux information that existed prior to the inversion and "posterior" refers to the information about the fluxes after the inversion. Prior and posterior information is modeled by multivariate Gaussian probability density functions (PDFs). The statistically optimal fluxes (i.e., the most likely fluxes, those that correspond to the maximum of the posterior PDF) are found by the iterative minimization of a cost function, following the principles of the four-dimensional variational (4D-Var) systems developed for numerical weather prediction [e.g., *Courtier et al.*, 1994]. A single inversion is performed that covers the 21 years at once.

[6] The operator that links the variables to be optimized (i.e., the surface fluxes) and the observations (i.e., the atmospheric measurements) in the inversion scheme is version 4 of the LMDZ transport model [*Hourdin et al.*, 2006], nudged to European Centre for Medium-Range Weather Forecasts (ECMWF; Reading, England) winds and in an off-line mode (transport mass fluxes are read from a frozen archive rather than being computed online). Tracer transport is simulated on a 3.75° × 2.5° (longitude-latitude) horizontal grid and with 19 layers between the surface and the top of the atmosphere. The LMDZ is part of the coupled climate model of Institut Pierre Simon Laplace. It has participated in a series of recent intercomparison exercises for the simulation of CO_2 mixing ratios [*Peylin et al.*, 2007; *Stephens et al.*, 2007; *Law et al.*, 2008; *Patra et al.*, 2008]. For numerical efficiency the inversion system makes use of the tangent-linear and the adjoint versions of the LMDZ, with possible updates of the linearization during the minimization. Note that the uncertainty of the LMDZ model is taken into account in the observation error budget, as described in section 2.2. In principle, the posterior PDF should therefore bear little sensitivity to the choice of that model versus models of the same generation. In practice, the results are affected by computation biases that may be model dependent [e.g., *Stephens et al.*, 2007].

[7] The 21 year inversion consisted of a 30 iteration minimization with the conjugate gradient algorithm of *Fisher and Courtier* [1995]. The whole minimization lasted 6 weeks with eight Itanium2 CPUs at 1.6 GHz running in parallel. Note that the inversion has been actually repeated in this configuration with synthetic data to compute the posterior error statistics, as explained at the end of this section. For the real measurements the minimization allowed the gradient of the cost function to be reduced by 4 orders of magnitude. As explained by *Chevallier et al*. [2007], the algorithm estimates the leading eigenvalues of the Hessian of the cost function as a by-product of the minimization. The condition number of the Hessian is given by the largest eigenvalue (here 10 million) and gives an indication of the rate of convergence. The smallest Hessian eigenvalue is unity, given the preconditioning used in the inversion system [*Chevallier et al.*, 2007]. The smallest one that is estimated by the 30 iteration minimization is 60. The degree of convergence can be evaluated in a complementary way. Indeed, in an optimal system the minimum value of the cost function is chi-square distributed with expectation and variance equal to the number of observations. In the idealized version of our system, which is described at the end of this section, the cost function starts at about 10,333,000 and reaches about 1,312,000 after 30 iterations, given about 1,202,000 observations. These two diagnostics mean that the convergence has not been fully reached, but most of it has been achieved.

[8] Our prior fluxes combine several information sources. Fossil fuel CO_2 emissions are from the EDGAR3.2 Fast Track 2000 emission database [*Olivier et al.*, 2001] scaled with the annual global totals of the Carbon Dioxide Information Analysis Center (http://cdiac.ornl.gov/ftp/ndp030/global.1751_2006.ems). Air-sea CO_2 exchange is prescribed from the climatology of air-sea CO_2 partial pressure difference by *Takahashi et al.* [2009]. The biosphere-atmosphere CO_2 fluxes over land are provided by the Organizing Carbon and Hydrology in Dynamic Ecosystems (ORCHIDEE) model described by *Krinner et al.* [2005]. The carbon-water-energy ORCHIDEE model explicitly simulates the principal processes of the continental biosphere influencing the fluxes of CO_2 exchanged with the atmosphere. The model handles short-term (half-hourly) to long-term (yearly and beyond) flux and pool variations. It is forced here by the atmospheric conditions given by the Interim Reanalysis of ECMWF (ERA-Interim [*Berrisford et al.*, 2009]). The ERA-Interim database starts in 1989, and conditions for year 1988 are repeated here from year 1989. ORCHIDEE fluxes used here are annually balanced at the start of the simulation and take neither land-use change nor wildfires into account. CO_2 released into the atmosphere by biomass burning is described by the Global Fire Emissions Database, Version 2 (GFEDv2 [*Randerson et al.*, 2007]) for the period after 1997. For the period 1988–1996 GFEDv2 has been extrapolated based on a regression of the GFEDv2 data set on the Cooperative Atmospheric Data Integration Project—Carbon Monoxide [*GLOBALVIEW-CO*, 2008] global growth rate, making the assumption that the CO growth rate interannual variability is determined entirely by biomass burning [*van der Werf et al.*, 2004; *Bousquet et al.*, 2006]. The fire fluxes are assigned to the LMDZ surface level. Burnt vegetation is assumed to recover rapidly: the mass of carbon emitted annually during specific fire events is compensated by a flux that is the same but of opposite sign distributed regularly throughout the year, so that the vegetation fluxes remain annually balanced.

[9] Prior information about the mixing ratios at the initial time step of the inversion window is also given to the system in the form of a (3D) field from a previous LMDZ simulation with climatological fluxes as boundary conditions. A global offset was added to this field so that the model fits the monthly mean of the Mauna Loa station (MLO) record for the first month of the inversion window, that is, January 1988.

[10] Prior fluxes are interpolated to the LMDZ 3.75° × 2.5° longitude-latitude grid with a 3 h temporal resolution. The flux increments on top of these prior fluxes are inferred at the same spatial resolution, but given significant temporal autocorrelations of the prior land biospheric fluxes at the scale of days [*Chevallier et al.*, 2006], the temporal resolution of the increments is reduced to 8 days, with daytime and nighttime separated. The 3D mixing ratio field at the start of the assimilation window (i.e., at 0000 on 1 January 1988) is also optimized, in the form of a 2D horizontal field (i.e., without any vertical resolution in the increments).

[11] As said before, the error statistics of the prior fluxes are modeled by a multivariate Gaussian distribution. The spatial variation of the error standard deviation at pixel level is illustrated in Figure 1a. Over land we assume that the errors of the ORCHIDEE model dominate the error budget and the parameters of the distribution are constrained by the comparison between in situ flux measurements and the outputs of a biosphere model that was reported by *Chevallier et al.* [2006]: temporal correlations on daily mean net carbon exchange (NEE) errors decay exponentially with a length of 1 month, but nighttime errors are assumed to be uncorrelated with daytime errors; spatial correlations decay exponentially with a length of 500 km (i.e., about the east-west size of the transport model grid at the equator); and standard deviations are set proportional to the heterotrophic respiration flux of ORCHIDEE (the scaling factor, deduced from an update of the NEE error analysis of *Chevallier et al*. [2006], at eddy covariance sites, is 2.3), with a ceiling of 3 gC m^{-2} per day. Over a full year the total 1σ uncertainty for all land fluxes amounts to about 3.6 GtC a^{-1}. The error statistics for the open ocean are more arbitrary and the following parameters have been chosen: temporal correlations decay exponentially with a length of 1 month; unlike land, daytime and night-time flux errors are correlated; spatial correlations follow an e-folding length of 1000 km; and standard deviations are set to 0.2 gC m^{-2} per day (for comparison, we found that the standard deviation of the differences between the air-sea flux climatology of *Takahashi et al.* [2009] and the fluxes computed from the individual pCO_2 measurements of the database of *Takahashi et al*. [2007] is 0.08 gC m^{-2} per day). With this setup the global air-sea flux uncertainty amounts to about 0.9 GtC a^{-1}. Land and ocean flux errors are not correlated. A 0.3% uncertainty is assigned to the total columns of CO_2 at the start of the assimilation window.

[12] Following *Chevallier et al*. [2007] we rely here on a Monte Carlo approach to estimate the error statistics of the inverted fluxes: these are reconstructed from an ensemble of inversions using synthetic data as input. The ensemble is defined in such a way that it rigorously explores the statistics of the prior errors and of the observation errors. In other words, if the ensemble of inversions grows, the corresponding ensemble of observations converges toward the assigned observation error statistics. The same feature applies to the ensemble of the prior fluxes that converge toward the assigned prior error statistics. By construction, the ensemble of the inverted fluxes then follows the theoretical error statistics of the posterior fluxes. This feature is exploited here with a synthetic 21 year inversion over the same period.

2.2. Assimilated Observations

[13] The surface measurements used as input to the inversion system are mixing ratios of CO_2 (expressed as dry mole fractions) either collected in flask air samples at various places in the world over land (from fixed sites) and over ocean (from commercial ships) or determined in situ by automatic analyzers. One hundred twenty-eight station records are used, which are described in Tables 1 and 2. Their location is shown in Figure 2. Three data sources, representing cooperative efforts from many laboratories around the globe, are exploited here: the NOAA ESRL archive (ftp://ftp.cmdl.noaa.gov/ccg/co2/), the CarboEurope atmospheric archive (http://ce-atmosphere.lsce.ipsl.fr/database/index_database.html), and the WDCGG archive (http://gaw.kishou.go.jp/cgi-bin/wdcgg/catalogue.cgi). Records from three additional stations were extracted from the LSCE database. All data have been downloaded on 28 September 2009. Differences in the measurement practices (sampling procedures, gas handling,

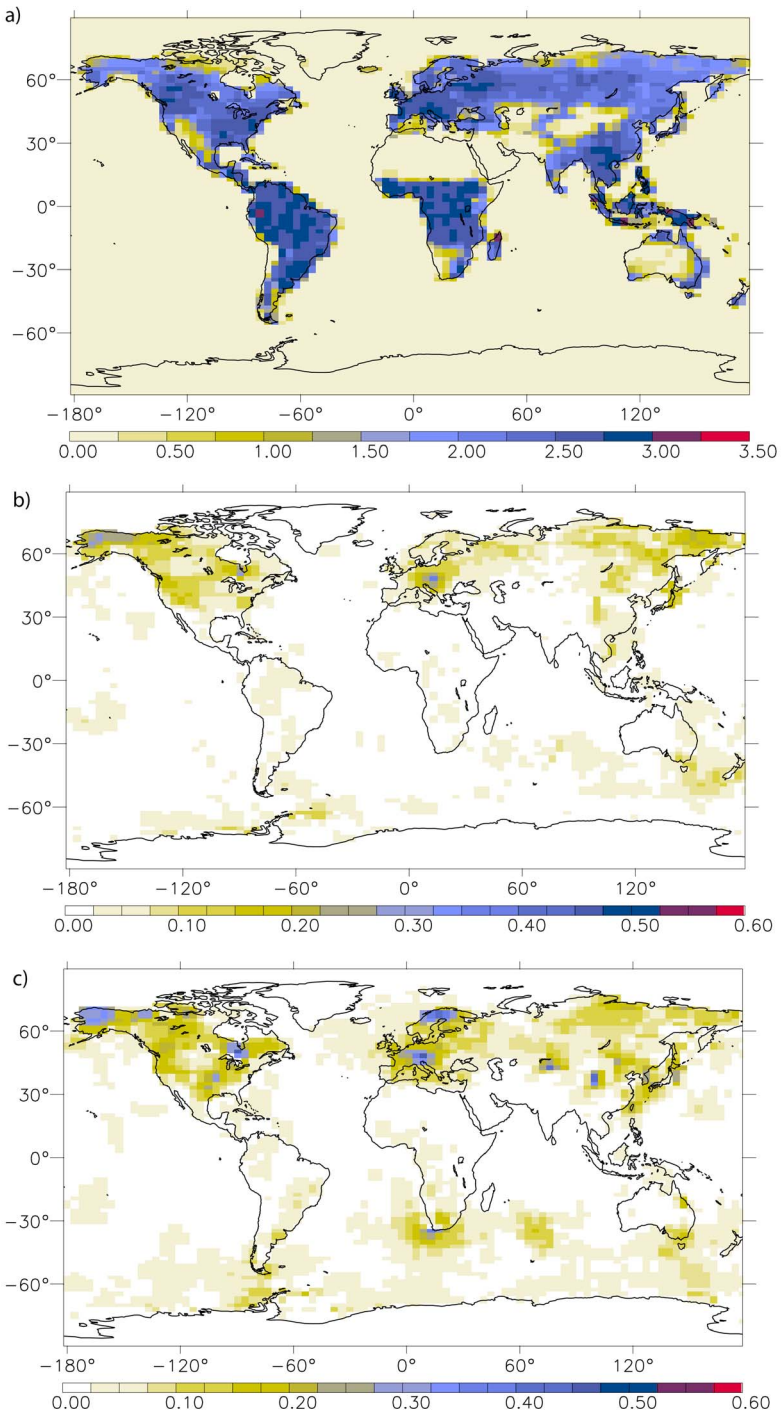

Figure 1. (a) Quadratic mean σ_b of the standard deviation of the errors of the prior weekly fluxes (gC m^{-2} per day) throughout the 21 years. Expected uncertainty reduction in each grid point provided by surface stations for estimation of 8-day-mean CO_2 surface fluxes for the periods (b) 1988–1997 and (c) 1998–2008. The reduction is defined as $[1 - (\sigma_a/\sigma_b)]$, with σ_a the quadratic mean of the posterior error standard deviation.

analytical procedures, calibration) between laboratories or even within the same laboratory over the 21 year period reduce the optimality of the inversion to some extent. It is hypothesized here that they are not an important error source for the inversion compared to the other ones, like those of the transport model [e.g., *Rödenbeck et al.*, 2006].

[14] Among all the station records, only those that spanned at least 5 years at the same location (or nearly the same location in the case of the neighboring BZH and LPO sites in Brittany), whether operated by the same agency or not, whether using the same measurement technique or not, were selected. When several measurement heights are reported for

Table 1. List of the Continuous Stations Used in This Study, the Period of Coverage, the Data Source, and the Contact Person[a]

Locality[b]	Period	Source	Contact
Alert, Nunavut, CA (ALT)	1988–2008	WDCGG/EC	D. Worthy
Amsterdam Island, FR (AMS)	1988–2008	LSCE	M. Ramonet
Anmyeon-do, KR (AMY)	1999–2007	WDCGG/KMA	Y. Youn
Barrow, Alaska, US (BRW)	1988–2008	NOAA ESRL	K. Thoning
Cabauw tower, 200 m level, NL (CBW0200)	2000–2008	CarboEurope/ECN	A. Vermeulen
Cape Ochi-ishi, JP (COI)	1995–2002	WDCGG/NIES	H. Mukai
Monte Cimone, IT (CMN)	1997–2005	CarboEurope/IAFMS	R. Santaguida
Cape Point, SA (CPT)	1993–2008	WDCGG/SAWS	E. Brunke
Frasedale, CA (FSD)	1990–2008	WDCGG/EC	D. Worthy
Hateruma, JP (HAT)	1993–2002	WDCGG/NIES	H. Mukai
Hegyhatsal tower, 115 m level, HU (HUN0115)	1997–2007	CarboEurope/HMS	L. Haszpra
Tenerife, Canary Islands, ES (IZO)	1988–2008	WDCGG/AEMET	A. J. Gomez-Pelaez
Jubany, Antartica, AR (JBN)	1994–2008	WDCGG/ISAC IAA	L. Ciattaglia
Jungfraujoch, CH (JFJ)	2005–2008	CarboEurope/Univ. Bern	M. Leuenberger
Kasprowy, PL (KAS)	2000–2007	CarboEurope/Univ. Poland	M. Zimnoch
Kotelny Island, RU (KOT)	1988–1993	WDCGG/MGO	N. Paramonova
K-puszta, HU (KPS)	1988–1999	WDCGG/HMS	L. Haszpra
Lampedusa, IT (LAM)	2001–2006	CarboEurope/ENEA	A. di Sarra
Park Falls, Wisconsin, US (LEF)	2003–2008	NOAA ESRL	A. Andrews
Mace Head, County Galway, IE (MHD)	1992–2008	CarboEurope/LSCE	M. Ramonet
Mauna Loa, Hawaii, US (MLO)	1988–2008	NOAA ESRL	K. Thoning
Minamitorishima, JP (MNM)	1993–2008	WDCGG/JMA	Y. Esaki
Pallas-Sammaltunturi, GAW Station, FI (PAL)	1998–2008	CarboEurope/FMI	T. Aalto
Plateau Rosa, IT (PRS)	1997–2007	CarboEurope/CESI RICERCA	F. Apadula
Puy de Dome, FR (PUY)	2001–2008	CarboEurope/LSCE	M. Ramonet
Ryori, JP (RYO)	1988–2008	WDCGG/JMA	Y. Esaki
Schauinsland, DE (SCH)	1997–2006	CarboEurope/Univ. Heidelberg	I. Levin
Tutuila, American Samoa (SMO)	1988–2008	NOAA ESRL	K. Thoning
Sonnblick, AU (SNB)	2000–2008	WDCGG/EEA	M. Fröhlich
South Pole, Antarctica, US (SPO)	1988–2008	NOAA ESRL	K. Thoning
Tsukuba tower, 200 m level, JP (TKB)	1992–2000	WDCGG/MRI	Y. Sawa
Westerland, DE (WES)	1997–2004	CarboEurope/Univ. Heidelberg	I. Levin
Moody, Texas, US (WKT)	2003–2008	NOAA ESRL	A. Andrews
Yonagunijima, JP (YON)	1997–2008	WDCGG/JMA	Y. Esaki
Zeppelin, Ny-Alesund, Svalbard, Norway and Sweden (ZEP)	2004–2007	CarboEurope/Stockholm Univ.	K. B. Noone

[a]Each station is identified by the name of the place, the corresponding country (abbreviated), and the code used in the corresponding database. The period of coverage is defined as the period between the first sample and the last one.
[b]The identifier is given in parentheses.

a given site such as at a tall tower, only the highest level was kept, being representative of mid-boundary layer mixing ratios, a signal easier to reproduce in global transport models than near-surface mixing ratios variability. Five selected sites from the WDCGG database were reported as daily means only (BER, CPT, CSJ, KOT) and one appeared as the monthly mean (BAR): they are used as such in the inversion system. The flask samples that were not blacklisted by the data providers are ingested individually in the model at the exact hour of their sampling. For continuous measurements the inversion system exploits the data from between 1200 and 2000 local solar time, except for high terrains (i.e., higher than 1000 m above sea level), where the data from between 0100 and 0600 local solar time are used. The temporal subset refers to the better performance of the models at these times [e.g., *Patra et al.*, 2008]. Subgrid-scale topography usually makes the real station heights differ from the model surface heights above sea level. The choice of the model vertical level assigned to a station is therefore somewhat arbitrary. We empirically chose the level close to the actual station height, that corresponds to 80% of the difference between the actual station height and the model surface height above sea level in the corresponding grid box.

[15] The uncertainty assigned to each observation within the inversion system includes the error of the measurement, the error of the forward model that simulates it from the fluxes, and the representation error (i.e., the mismatch between the scale of the measurement and the scale of the transport model). It is time independent here: its variance is set to half the variance of the high-frequency variability of the deseasonalized and detrended CO_2 time series of the measurement at a given station (even for the five stations where the data are provided as daily or monthly averages). The high-frequency variability is calculated following *Masarie and Tans* [1995]. The resulting error varies between a few tenths of a part per million for marine stations and several parts per million for continental ones, reaching 6 ppm at CBW0200 station, in the Netherlands, that is, more than 1 order of magnitude larger than the measurement errors. Because of the large temporal error correlations of the transport models that simulate the measurements in the flux inversion systems [*Lauvaux et al*. 2009b], the continuous measurements have been further deweighted by multiplying the observation error by the square root of the number of local data within the selected local time range. Error correlations are therefore neglected.

[16] The measurements have been screened automatically for the inversion by comparison with the mole fractions calculated by LMDZ from the prior fluxes: 5% of the individual measurements for which the detrended and deseasonalized

Table 2. Same as Table 1, but for Flask-Sampling Stations[a]

Locality	Period	Source	Contact
Alert, Nunavut, CA (ALT)	1988–2008	NOAA/ ESRL	T. Conway
Amsterdam Island, FR (AMS)	1988–1990	NOAA/ ESRL	T. Conway
Amsterdam Island, FR (AMS)	2003–2008	LSCE	M. Ramonet
Ascension Island, GB (ASC)	1988–2008	NOAA/ ESRL	T. Conway
Assekrem, DZ (ASK)	1995–2008	NOAA/ ESRL	T. Conway
Terceira Island, Azores, PT (AZR)	1988–2008	NOAA/ ESRL	T. Conway
Baltic Sea, PL (BAL)	1992–2008	NOAA/ ESRL	T. Conway
Baring Head, NZ (BAR)	1988–1998	WDCGG/ NIWA	A. Gomez
Bering Island, RU (BER)	1988–1994	WDCGG/ MGO	N. Paramonova
Begur, ES (BGU)	2000–2008	CarboEurope/IC·3 / LSCE	J. A. Morguí, X. Rodó
Baring Head, NZ (BHD)	1999–2008	NOAA/ESRL	T. Conway
St. Davids Head, Bermuda, GB (BME)	1989–2008	NOAA/ ESRL	T. Conway
Tudor Hill, Bermuda, GB (BMW)	1989–2008	NOAA/ ESRL	T. Conway
Barrow, Alaska, US (BRW)	1988–2008	NOAA/ ESRL	T. Conway
Portsall, FR (BZH)	1998–2001	CarboEurope/LSCE	M. Ramonet
Cold Bay, Alaska, US (CBA)	1988–2007	NOAA/ ESRL	T. Conway
Cape Ferguson, AU (CFA)	1991–2008	WDCGG/ CSIRO	P. Krummel, R. Langenfelds, P. Steele
Cape Grim, Tasmania, AU (CGO)	1988–2008	NOAA/ ESRL	T. Conway
Christmas Island, Republic of Kiribati (CHR)	1988–2008	NOAA/ ESRL	T. Conway
Cape Meares, Oregon, US (CMO)	1988–1998	NOAA/ ESRL	T. Conway
Crozet Island, FR (CRZ)	1991–2008	NOAA/ ESRL	T. Conway
Cape St. James, CA (CSJ)	1988–1992	WDCGG/ EC	D. Worthy
Casey Station, AU (CYA)	1997–2008	WDCGG/ CSIRO	P. Krummel, R. Langenfelds, P. Steele
Easter Island, CL (EIC)	1994–2008	NOAA/ ESRL	T. Conway
Estevan Point, British Columbia, CA (ESP)	1992–2005	WDCGG/ EC	D. Worthy
Finokalia, Crete, GR (FIK)	1999–2008	CarboEurope/ LSCE	M. Ramonet
Mariana Islands, Guam (GMI)	1988–2008	NOAA/ ESRL	T. Conway
Halley Station, Antarctica, GB (HBA)	1990–2008	NOAA/ ESRL	T. Conway
Hegyhatsal, HU (HUN)	1993–2008	NOAA/ ESRL	T. Conway
Storhofdi, Vestmannaeyjar, IS (ICE)	1992–2008	NOAA/ ESRL	T. Conway
Grifton, North Carolina, US (ITN)	1992–1999	WDCGG/ ESRL	T. Conway
Tenerife, Canary Islands, ES (IZO)	1991–2008	NOAA/ ESRL	T. Conway
Jungfraujoch, CH (JFJ)	2000–2008	CarboEurope/ Univ. of Bern	M. Leuenberger
Key Biscayne, Florida, US (KEY)	1988–2008	NOAA/ ESRL	T. Conway
Cape Kumukahi, Hawaii, US (KUM)	1988–2008	NOAA/ ESRL	T. Conway
Sary Taukum, KZ (KZD)	1997–2008	NOAA/ ESRL	T. Conway
Plateau Assy, KZ (KZM)	1997–2008	NOAA/ ESRL	T. Conway
Lampedusa, IT (LAM)	2001–2007	CarboEurope/ ENEA	A. di Sarra
Ile grande, FR (LPO)	2005–2008	CarboEurope/ LSCE	Ramonet
Mawson, AU (MAA)	1990–2008	WDCGG/ CSIRO	P. Krummel, P. Steele, R. Langenfelds
Mould Bay, Nunavut, CA (MBC)	1988–1997	NOAA/ ESRL	T. Conway
Mace Head, County Galway, IE (MHD)	1991–2008	NOAA/ ESRL	T. Conway
Mace Head, County Galway, IE (MHD)	1996–2008	CarboEurope/ LSCE	M. Ramonet
Sand Island, Midway, US (MID)	1988–2008	NOAA/ ESRL	T. Conway
Mauna Loa, Hawaii, US (MLO)	1988–2008	NOAA/ ESRL	T. Conway
Macquarie Island, AU (MQA)	1990–2008	WDCGG/ CSIRO	P. Krummel, P. Steele, R. Langenfelds
Gobabeb, NA (NMB)	1997–2008	NOAA/ ESRL	T. Conway
Niwot Ridge, Colorado, US (NWR)	1988–2008	NOAA/ ESRL	T. Conway
Pallas-Sammaltunturi, GAW Station, FI (PAL)	2002–2008	NOAA/ ESRL	T. Conway
Pic du Midi, FR (PDM)	2001–2008	CarboEurope/ LSCE	M. Ramonet
Pacific Ocean, 0N (POC000)	1988–2008	NOAA/ ESRL	T. Conway
Pacific Ocean, 5N (POCN05)	1988–2008	NOAA/ ESRL	T. Conway
Pacific Ocean, 10N (POCN10)	1988–2008	NOAA/ ESRL	T. Conway
Pacific Ocean, 15N (POCN15)	1988–2008	NOAA/ ESRL	T. Conway
Pacific Ocean, 20N (POCN20)	1988–2008	NOAA/ ESRL	T. Conway
Pacific Ocean, 25N (POCN25)	1988–2008	NOAA/ ESRL	T. Conway
Pacific Ocean, 30N (POCN30)	1988–2008	NOAA/ ESRL	T. Conway
Pacific Ocean, 5S (POCS05)	1988–2008	NOAA/ ESRL	T. Conway
Pacific Ocean, 10S (POCS10)	1988–2008	NOAA/ ESRL	T. Conway
Pacific Ocean, 15S (POCS15)	1988–2008	NOAA/ ESRL	T. Conway
Pacific Ocean, 20S (POCS20)	1988–2008	NOAA/ ESRL	T. Conway
Pacific Ocean, 25S (POCS25)	1988–2008	NOAA/ ESRL	T. Conway
Pacific Ocean, 30S (POCS30)	1988–2008	NOAA/ ESRL	T. Conway
Palmer Station, Antarctica, US (PSA)	1988–2008	NOAA/ ESRL	T. Conway
Point Arena, California, US (PTA)	1999–2008	NOAA/ ESRL	T. Conway
Puy de Dome, FR (PUY)	2001–2008	CarboEurope/ LSCE	M. Ramonet
Ragged Point, BB (RPB)	1988–2008	NOAA/ ESRL	T. Conway
Schauinsland, DE (SCH)	1997–2006	CarboEurope/ Univ. Heidelberg	I. Levin
South China Sea, 3N (SCSN03)	1991–1998	NOAA/ ESRL	T. Conway
South China Sea, 6N (SCSN06)	1991–1998	NOAA/ ESRL	T. Conway
South China Sea, 9N (SCSN09)	1991–1998	NOAA/ ESRL	T. Conway
South China Sea, 12N (SCSN12)	1991–1998	NOAA/ ESRL	T. Conway

Table 2. (continued)

Locality	Period	Source	Contact
South China Sea, 15N (SCSN15)	1991–1998	NOAA/ ESRL	T. Conway
South China Sea, 18N (SCSN18)	1991–1998	NOAA/ ESRL	T. Conway
South China Sea, 21N (SCSN21)	1991–1998	NOAA/ ESRL	T. Conway
Mahe Island, SC (SEY)	1988–2008	NOAA/ ESRL	T. Conway
Southern Great Plains, Oklahoma, US (SGP)	2002–2008	NOAA/ ESRL	T. Conway
Shemya Island, Alaska, US (SHM)	1988–2008	NOAA/ ESRL	T. Conway
Ship between Ishigaki Island and Hateruma Island, JP (SIH)	1993–2005	WDCGG/ Tohoku University	T. Nakazawa
Tutuila, American Samoa (SMO)	1988–2008	NOAA/ ESRL	T. Conway
South Pole, Antarctica, US (SPO)	1988–2008	NOAA/ ESRL	T. Conway
Ocean Station M, NO (STM)	1988–2008	NOAA/ ESRL	T. Conway
Summit, GL (SUM)	1997–2008	NOAA/ ESRL	T. Conway
Syowa Station, Antarctica, JP (SYO)	1988–2008	NOAA/ ESRL	T. Conway
Tae-ahn Peninsula, KR (TAP)	1991–2008	NOAA/ ESRL	T. Conway
Tierra Del Fuego, Ushuaia, AR (TDF)	1994–2008	NOAA/ ESRL	T. Conway
Trinidad Head, California, US (THD)	2002–2008	NOAA/ ESRL	T. Conway
Tromelin Island, F (TRM)	1998–2007	LSCE	M. Ramonet
Wendover, Utah, US (UTA)	1993–2008	NOAA/ ESRL	T. Conway
Ulaan Uul, MN (UUM)	1992–2008	NOAA/ ESRL	T. Conway
Sede Boker, Negev Desert, IL (WIS)	1996–2008	NOAA/ ESRL	T. Conway
Mt. Waliguan, CN (WLG)	1991–2008	NOAA/ ESRL	T. Conway
Ny-Alesund, Svalbard, Norway and Sweden (ZEP)	1994–2008	NOAA/ ESRL	T. Conway

[a]Station BHD in the NOAA ESRL archive is known as BAR in the WDCGG database.

departure with the model was larger than 3 observation-error standard deviations were conservatively rejected, because the transport model may not able to reproduce some local signals.

[17] Comparing the station map in Figure 2 and the error map in Figure 1a, it is noteworthy that some of the regions where the prior fluxes are the most uncertain, like the western part of Russia and the tropical lands, are station void. CO_2 fluxes there should still be improved by the inversion because they influence the mixing ratios measured in other parts of the world to some extent, but the inversion cannot significantly reduce their uncertainty. This is quantified in section 4.1.

3. Validation Method

3.1. Independent Observations

[18] Given their relatively coarse spatial resolution (3.75° × 2.5° longitude-latitude), the inverted fluxes cannot be directly

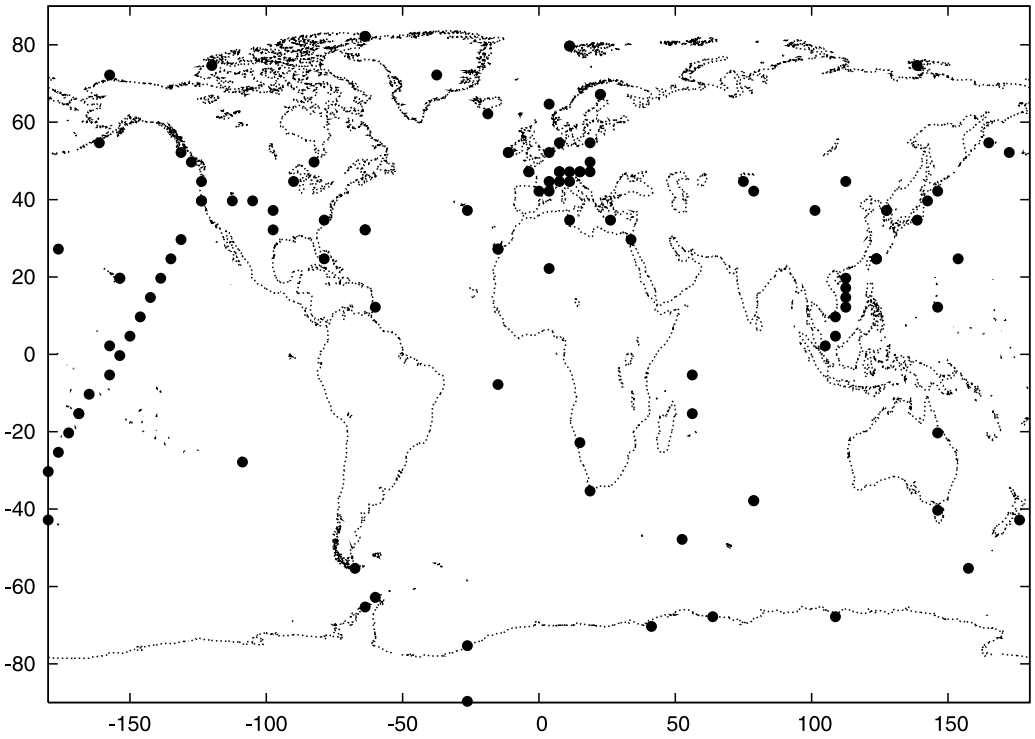

Figure 2. Location of the surface stations used in this study.

Table 3. Characteristics of the 34 Aircraft Campaigns From the GEOMON CO_2 Airborne Data Archive

Mission	Location	Period	Organization	Principal Investigator
AASE-II	North Arctic, North America, Eastern Pacific	Jan–Mar 1992	NASA	B. Anderson
AIA	North East Tasmania, Australia	Jun 1991–Sep 2000	CSIRO	P. Steele
BIBLE-A	Western Pacific	Sep 1998	NIES	T. Machida
BIBLE-B	Western Pacific	Aug 1999	NIES	T. Machida
BIBLE-C	Western Pacific	Nov 2000	NIES	T. Machida
CAR	Eastern Colorado, USA	Nov 1992–Dec 2002	NOAA	P. Tans, C. Sweeney
COBRA-2000	North America	Jul–Aug 2000	Harvard Univ.	S. Wofsy
COBRA-2003	North America	May–Jun 2003	Harvard Univ.	S. Wofsy
COBRA-2004	North America	May–Aug 2004	Harvard Univ.	S. Wofsy
CRYSTAL	Southern North America, Caribbean	May–Jul 2002	Harvard Univ.	S. Wofsy
FTL	Northern Brazil	Dec 2000–Jul 2002	NOAA	P. Tans, C. Sweeney
HAA	Hawaii, USA	May 1999–Dec 2002	NOAA	P. Tans, C. Sweeney
HFM	Northeast United States	Nov 1999–Nov 2002	NOAA	P. Tans, C. Sweeney
INTEX-NA	North America	Jul–Aug 2004	NASA	S. Vay
LEF	Northern Central United States	Apr 1998–Dec 2002	NOAA	P. Tans, C. Sweeney
PEM-TROP-A-DC8	South Pacific Basin	Sep–Oct 1996	NASA	S. Vay
PEM-TROP-A-P3B		Aug–Sep 1996	NASA	B. Anderson
PEM-TROP-B-DC8	South Pacific Basin	Mar–Apr 1999	NASA	S. Vay
PEM-TROP-B-P3B	South Pacific Basin	Mar–Apr 1999	NASA	S. Vay
PEM-WEST-A	Western Pacific Basin, North of Equator	Sep–Oct 1991	NASA	B. Anderson
PEM-WEST-B	Western and Eastern Pacific Basin, North of Equator	Feb–Mar 1994	NASA	B. Anderson
PFA	Alaska, United States	Jun 1999–Dec 2002	NOAA	P. Tans, C. Sweeney
POLARIS	Northwest Pacific, Alaska and the Arctic	Apr–Sep 1997	Harvard Univ.	S. Wofsy
PRE-AVE	North America	Jan 2004	Harvard Univ.	S. Wofsy
RTA	Rarotonga, South Pacific	Apr 2000–Dec 2002	NOAA	P. Tans, C. Sweeney
SAN	Northern Brazil	Dec 2000–May 2002	NOAA	P. Tans, C. Sweeney
SOLVE-DC8	Arctic	Nov 1999–Mar 2000	NASA	S. Vay
SONEX		Oct–Nov 1997	NASA	B. Anderson
STRAT	Western North America, Northeast Pacific	May–Dec 1995/1996	Harvard Univ.	S. Wofsy
SUCCESS	Midwestern USA to North Pacific	Apr–May 1996	NASA	S. Vay
TOTE-VOTE	Midwestern USA	Dec–Feb 1995/1996	NASA	B. Anderson
TRACE-A-DC8	Arctic and Eastern South Pacific	Sep–Oct 1992	NASA	B. Anderson
TRACE-P-DC8	North Pacific Basin	Mar–Apr 2001	NASA	S. Vay
TRACE-P-P3B	North Pacific Basin	Mar–Apr 2001	NASA	S. Vay

compared to flux measurements that are representative of much smaller scales. Only indirect comparisons with independent mixing ratio measurements can be studied for the evaluation. In this study, aircraft data have been gathered for this purpose. They have not been exploited by the inversion system and have been left aside for validation. Two databases have been merged for validation purpose. The first one is the CO_2 Airborne Data Archive. This database, containing publicly available CO_2 and CH_4 airborne data from more than 50 separate measurement campaigns, of which 34 are used here, was created as part of the ongoing European Union-funded project GEOMON (http://www.geomon.eu/). Information related to the specific aircraft data used here is listed in Table 3. The second archive comes from the CONTRAIL project [*Machida et al.*, 2008] that is being jointly conducted by the NIES (National Institute for Environmental Studies), the MRI (Meteorological Research Institute), JAL (Japan Airlines International), JAMCO (JAMCO Corporation), and JAL-F (JAL Foundation). CONTRAIL gathers commercial-aircraft-based observations for the period since November 2005. Data from takeoff and landing at 45 airports in the world are used here.

3.2. Benchmarking Using a Poor Man's Inversion

[19] The improvement brought by a flux inversion on the simulation of mixing ratios usually looks impressive because the inversion easily corrects the growth rate of CO_2. But, since the global trend can be accurately obtained from just a few marine surface sites, like MLO and SPO, it is important to assess whether inverted fluxes actually capture more information than this trend. In other words, we may wonder whether all the stations exploited here bring some constraint on the flux distribution that is superior to the global trend from MLO and SPO. For this purpose, *Chevallier et al.* [2009] introduced a baseline inversion that they called the "poor man's method," against which more sophisticated inversions can be benchmarked. In this baseline (which is slightly simplified here), the ocean fluxes are kept identical to the prior ones. Over land the poor man's flux F_{pm} at location (x,y) and at time t is defined as

$$F_{\mathrm{pm}}(x,y,t) = F_{\mathrm{prior}}(x,y,t) + k(\mathrm{year}) \times \sigma(x,y,t). \qquad (1)$$

$F_{\mathrm{prior}}(x,y,t)$ is the prior flux at the same time and location. $\sigma(x,y,t)$ is its uncertainty, that is, the standard deviation of the prior error described in section 2.1. k(year) is a coefficient that varies as a function of the year only. k is chosen here so that the mean annual global totals of the poor man's fluxes equal the mean global totals given by the annual global CO_2 growth rate from the *GLOBALVIEW-CO_2* [2009] product multiplied by a conversion factor (2.12 GtC a^{-1} per ppm [*Denman et al.*, 2007, Table 7.1]). In practice, this simple approach distributes the land carbon sink according to the heterotrophic respiration fluxes from the vegetation without

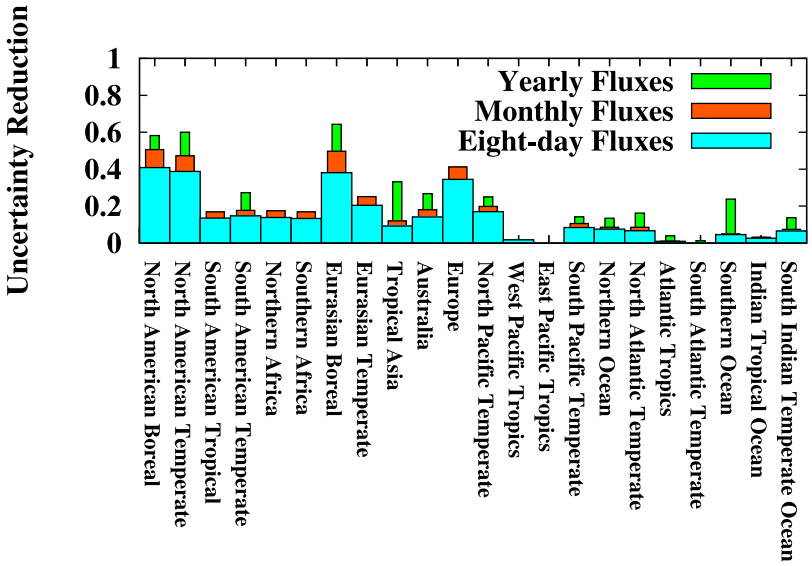

Figure 3. Expected uncertainty reduction provided by surface stations for estimation of CO_2 surface fluxes in the 22 TransCom3 regions for the period 1988–2008. As in Figure 1 the error reduction is defined as $[1 - (\sigma_a/\sigma_b)]$, with σ_a the posterior error standard deviation and σ_b the prior error standard deviation. Results for weekly (blue bars), monthly (red bars), and annual (green bars) fluxes are shown. Note that for annual fluxes, σ_a and σ_b are computed on an ensemble of 21 realizations of the yearly errors only.

any spatial information from the atmospheric observations or any temporal information within any given year.

4. Results

4.1. Information Content

[20] As explained by *Chevallier et al.* [2007], our Monte Carlo approach yields an estimate of the degree of freedom for signal (DOFS) of the observation system. The DOFS quantifies the number of independent quantities about the fluxes that the inversion system exploits. In the present case it is about 400 per year.

[21] The distribution of the fractional uncertainty reduction over the globe (Figures 1b and 1c) shows where in space the 400 information pieces lie. Further, these maps quantify the knowledge brought by the surface measurements on the CO_2 weekly surface fluxes for the first (1988–1997) and second (1998–2008) decades of the study. The fractional uncertainty reduction is defined as 1 minus the ratio of the posterior error standard deviation to the prior error standard deviation. A value of 0 indicates that the observations have not provided any information to the prior. A value of 1 would be reached if the observations gave a perfect knowledge about the fluxes. The impact of the measurements results from the combination of assigned prior errors, assigned observation errors, observation density, and transport characteristics. It is mostly located in the vicinity of the stations, with values larger than 30% at continuous stations like FSD in eastern Canada, CPT in South Africa, and PAL in Finland. The values in Europe are consistent with those given in a previous study of the same kind by *Carouge et al.* [2008]. The difference between Figure 1b and Figure 1c mainly reflects the evolution of the network between the two decades, with several stations added to the network, like CPT in South Africa and PAL in Finland, and a few removed, like KOT in northern Russia. The MLO observatory does not appear to reduce flux errors in its vicinity despite its long continuous measurements, likely because the beneficial impact of MLO spreads over the whole globe. This illustrates the fact that MLO is an excellent choice for characterizing the signal of the global flux. The uncertainty reduction in the vicinity of flask stations, like KOT in northern Siberia, is usually about 10%. The impact appears to be larger when the fluxes solved in each grid point and 8 day period are aggregated in space and time. Figure 3 presents it at the scale of the widely used 22 TransCom3 regions of *Gurney et al.* [2002] and for weekly, monthly, and yearly averages for the second decade. In the mid- and high latitudes of the Northern Hemisphere lands, where most stations are located, all regional flux estimates are improved by more than 20% and by up to 60% (North American Boreal, North American Temperate, and Eurasian Boreal regions with annual fluxes). As an example, for the TransCom3 "Europe" region the inversion theoretically reduces the flux uncertainty from 1.0 to 0.6 GtC a^{-1}. The figures for the lands in the tropics and in the Southern Hemisphere are between 10 and 30%. Over ocean basins the reduction lies between 0 and 25%.

4.2. Comparison With Dependent Surface Measurements

[22] Figure 4 displays the root-mean-square (RMS) statistics between the LMDZ simulation and the surface measurements exploited in the inversion. The LMDZ simulation uses either the inverted fluxes or the poor man's fluxes as boundary conditions. The inversion is systematically better than the poor man. It fits all observations about their assigned uncertainty (ordinate in Figure 4b). Additional iterations to the inversion minimization would further reduce the RMS. Since the poor man does not exploit the individual

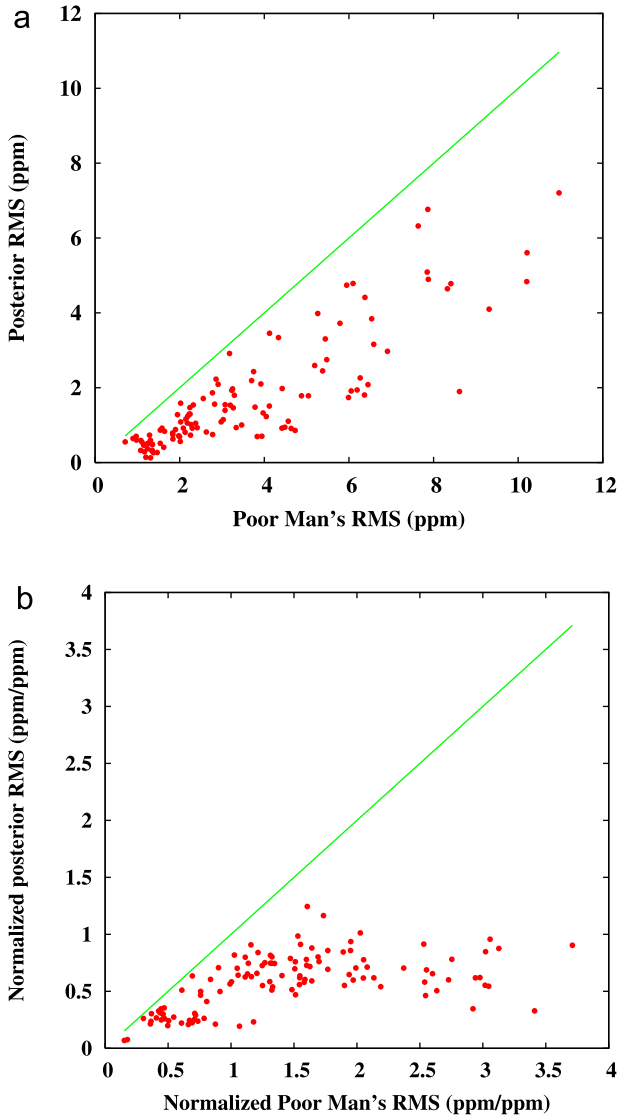

Figure 4. (a, b) RMS differences between the transport model of the Laboratoire de Météorologie Dynamique (LMDZ) simulations and individual surface measurements exploited in the inversion. LMDZ simulations use poor man's fluxes (abscissa) or posterior fluxes (ordinate) as boundary conditions. In Figure 4b, RMS values are normalized with the observation error assigned to each station in the inversion. Red circles represent measurement sites listed in Tables 1 and 2. The inversion performs better than the poor man's method at a given station when the corresponding circle is located under the bisector (green line).

measurements, it is less able than the full inversion to fit them within their assigned uncertainty: the model-minus-observation RMS exceeds the observation standard deviation by up to a fourfold factor for the poor man's simulation (abscissa in Figure 4b). However, it is usually outperformed by the full inversion by less than 4 ppm (Figure 4a). It is not obvious that this modest advantage seen in the dependent observations for the full inversion compared to the poor man's method holds for independent measurements. This is studied in section 4.4 after the analysis of the flux time series.

4.3. Flux Time Series

[23] The annual fluxes before and after the inversion are shown in Figure 5, aggregated at the scale of the 11 TransCom3 land regions. To interpret those fluxes, their uncertainty appears in Figure 5 in the form of error standard deviations, and the correlations between the uncertainties of the posterior fluxes are reported in Figure 6. Negative correlations express some ambiguity between the regional fluxes as seen by the observation network: North American Boreal vs. North American Temperate (−0.25), Southern Africa vs. Northern Africa (−0.24), and Europe vs. Eurasian Boreal (−0.31) or vs. Eurasian Temperate (−0.31). These correlations between the errors of aggregated fluxes imply that the interpretation of the high-resolution flux increments (8 days and 3.75° × 2.5°; see Figure 7 for an example) is particularly difficult. The high resolution of the inversion is important for proper representation of the prior errors, of the observation errors, and of the transport, but inverted carbon budgets are more reliable when aggregated.

[24] The inversion spreads a sink of a few GtC a^{-1} over the lands (Figure 5a) to yield the CO_2 growth rate seen by the measurements. This large negative increment varies in space and in time. For instance, in the North American Boreal region, the mean budget remains around 0 throughout the years before and after the inversion, while the inversion reduces the North American Temperate budget by a few tenths of a GtC a^{-1} without a noticeable trend and increases a positive trend in the Eurasian Temperate region. Some of the interannual variations are significantly changed, for instance, in the North American Temperate region and the region "Europe" between 1995 and 1998 and in the South American Tropical region before 2000. In the case of Europe the anomaly arises in its eastern part, which is both very uncertain in the prior budget (Figure 1a) and station void (Figure 2). Therefore the location of that increment could well be placed in Eurasia instead of Europe (Figure 6). Extension of the observation network toward eastern Europe and Siberia would be needed to resolve this ambiguity. The interannual variations of the increments may also include some artifacts

Figure 5. Time series of annual net CO_2 fluxes (a) for all lands and (b-l) in the 11 TransCom3 land regions. In the sign convention, positive fluxes correspond to a net carbon source into the atmosphere. The solid (black) line corresponds to the prior fluxes (including fossil fuel), while the posterior flux time series (including fossil fuel) is represented by the dotted (blue) line. Blue squares represent the posterior fluxes with fossil fuel subtracted. Shaded areas show the 68% confidence interval, as 1 standard deviation around the prior fluxes (beige) and around the posterior fluxes (overlaid in violet). Prior and posterior standard deviations are from the ensemble used for Figure 3. Since the ensemble contains only 21 members, standard deviations would be underestimated if it was not inflated here per region by the ratio between the true prior standard deviation (computed by summing all the terms in the prior error covariance matrix) and that of the ensemble. The ratio varies between 1 and 1.4 depending on the region.

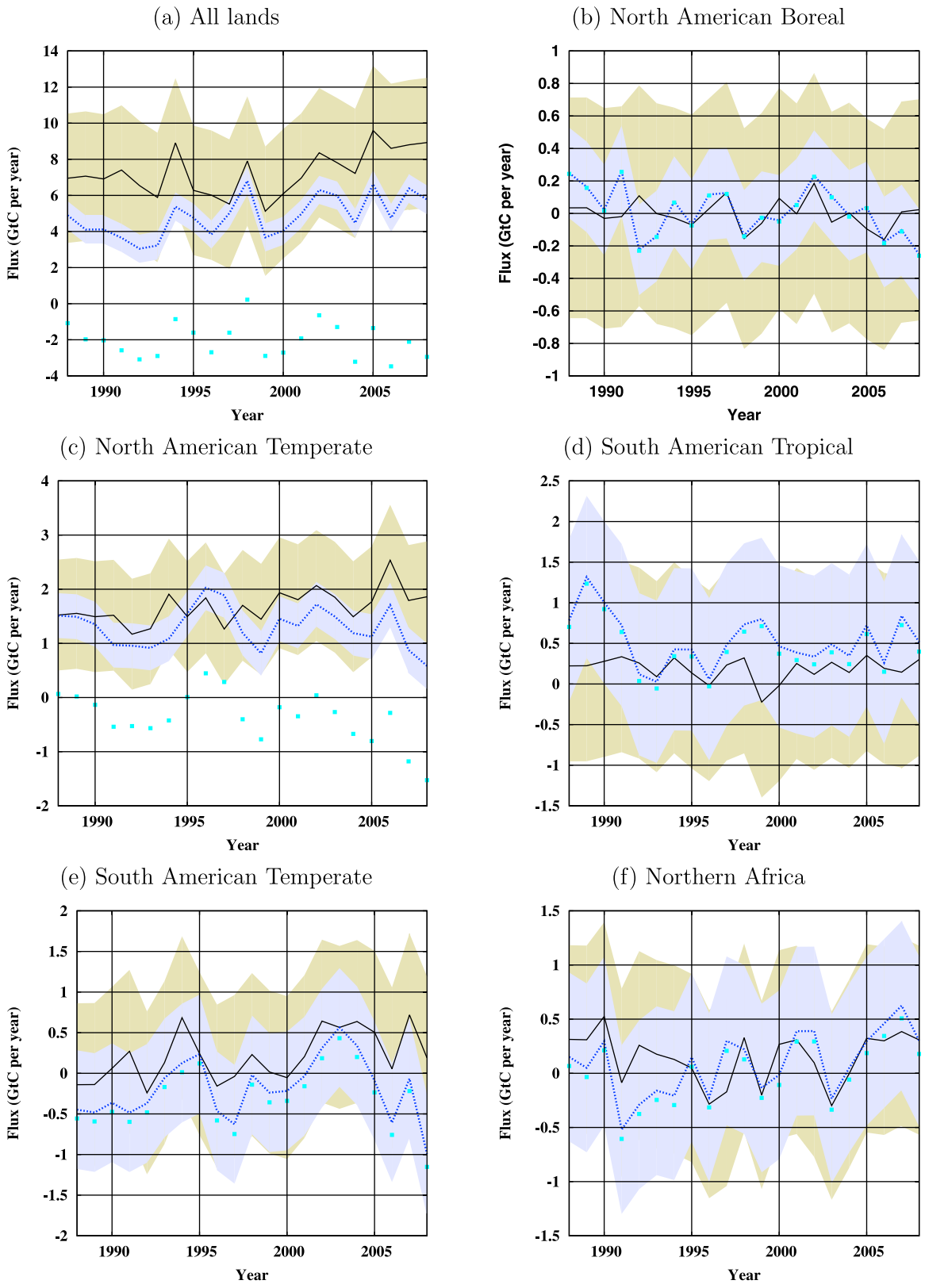
(a) All lands
(b) North American Boreal
(c) North American Temperate
(d) South American Tropical
(e) South American Temperate
(f) Northern Africa
Flux (GtC per year)
Year
1990
1995
2000
2005

Figure 5

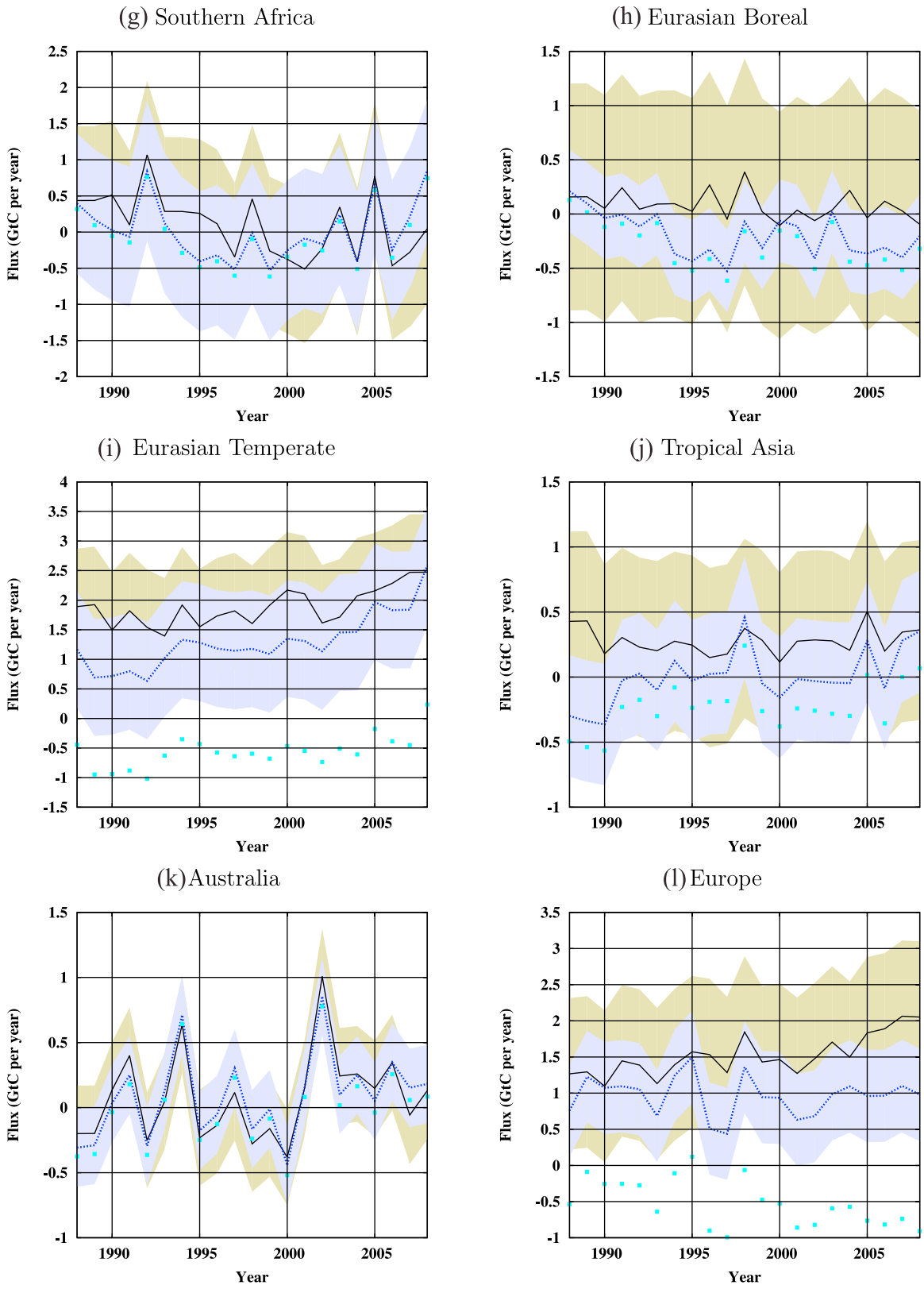

Figure 5. (continued)

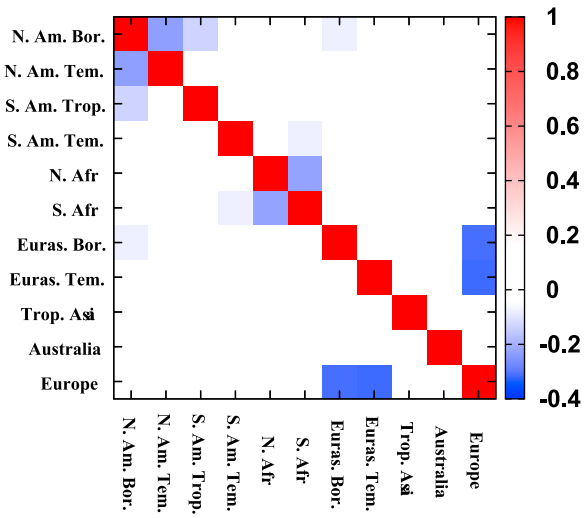

Figure 6. Correlations between the posterior uncertainties of the monthly regional fluxes aggregated at the scale of the 11 Transcom3 land regions, as computed from the ensemble used for Figure 3. Names are abbreviated. Correlations computed for yearly fluxes were found to be hardly reliable because the size of the ensemble in this case (21 members) is too small, but we expect that they behave similarly to the monthly flux correlations shown here.

induced by the variations of the measurement network during the 21 years (Tables 1 and 2). For instance, the introduction or even the momentary interruption of a station always changes the flux increments in its vicinity. It therefore affects the regional budgets, even remotely, because the inversion conserves the global mass budget from the first station onward.

[25] After the inversion, the net sources of CO_2 over land are mostly distributed in the temperate latitudes of the Northern Hemisphere (North American Temperate, Eurasian Temperate, and Europe regions) and in some of the tropics (South American Tropical and Northern Africa regions), while Eurasia Boreal and South American Temperate are identified as net sinks. The North American Boreal Region is about neutral. Without accounting for fossil fuel emissions (blue squares in Figure 5), most regions are sinks or neutral. The largest positive trends in the inverted net fluxes over the 21 years are seen in the Eurasian Temperate (+63 MtC a^{-1}), Northern Africa (+24 MtC a^{-1}), and Tropical Asia (+20 $MtCa^{-1}$) regions, while noticeable negative trends occur in the Eurasian Boreal (−17 MtC a^{-1}) region only.

[26] Figure 8 shows that the inversion significantly modifies the average seasonal cycle of the emissions over land, with a shift by 1 month and a global peak-to-peak amplitude smaller by about one third. The reduction in the amplitude may correct a weakness of the version of the ORCHIDEE model that is used here to provide the prior fluxes of the natural biosphere. This version of ORCHIDEE is not nitrogen limited and therefore may overestimate vegetation productivity and the seasonal cycle of the CO_2 flux. Other factors such as an insufficient summer water stress could play a role as well.

[27] The curves for the ocean basins are not shown because the inversion changes them to a negligible extent compared to their uncertainty (Figure 1a). As mentioned in the last paragraph of section 2.2, this feature is related to the large error budget of the prior fluxes over land relative to the ocean. The Bayesian inversion conservatively concentrates the increments in the most uncertain regions.

4.4. Comparison with Independent Aircraft Measurements

[28] The comparison with the validation aircraft measurements is summarized in Figure 9. Distinction is made between the statistics for the pointwise measurements within the 300–850 and 850–990 hPa layers. Note that the filled circles and squares represent 1 of the 34 aircraft campaigns listed in Table 3 and a series of takeoff and landing CONTRAIL measurements at a specific airport, respectively, without any distinction regarding either the length of the record or its spatial coverage. Figure 9b shows that within the lower layer, the poor man's method already keeps the fit of the atmospheric simulation to the aircraft measurements within 6 ppm (RMS) in most cases. The full inversion improves the fit (by up to 4 ppm) in most cases (consistent with the dependent measurements; see Figure 4) but degrades it by up to 3 ppm in 11 (mainly from the regular CONTRAIL measurements, which may be polluted by local urban emissions) of 79 cases. A possible contributing factor to the scatter may be the sole use of pressure altitude in our atmospheric computations, since it is independent of topography. The measurements in the free troposphere are representative of larger areas and the RMS statistics are consequently better, as shown in Figure 9a, for both the full inversion and the poor man. Even though the scatter of the RMS for the poor man's method hardly exceeds 4 ppm, the full inversion usually outperforms the poor man's method, by up to 2 ppm. This improvement with respect to high-altitude measurements occurs despite possible deficiencies in the modeling of vertical transport [*Stephens et al.*, 2007], which reinforces our confidence in the quality of the inverted fluxes. Both methods consistently produce large RMS values in a few cases: the RMS reaches about 12 ppm for the PEM-WEST-A (northern Pacific) and the LEF (USA) campaigns. The large improvement in the RMS by the inversion system compared to the poor man's method is caused by a smaller standard deviation rather than by a smaller bias (which is not larger either; not shown), as expected from the design of the poor man's method.

5. Conclusions

[29] The inversion of carbon fluxes has a recent but high-profile history [e.g., *Bousquet et al.*, 2000; *Gurney et al.*, 2002; *Le Quéré et al.*, 2007]. Compared to regional carbon inventories, inverse carbon flux estimates offer the advantage of better time-space consistency while providing global higher-time-space-resolution products. In principle, they could serve as independent references for some carbon trading scheme that would include the natural biosphere. They could also contribute to defining mitigation strategies by identifying the large natural sources and sinks over the globe for, respectively, reduction and protection/enhancement. Their spatial resolution has been too coarse for them to be validated against ground-truth measurements of surface fluxes yet, except in the mesoscale study by *Lauvaux et al.* [2009a] in the southwest of France, where some positive impact of the inversion was demonstrated.

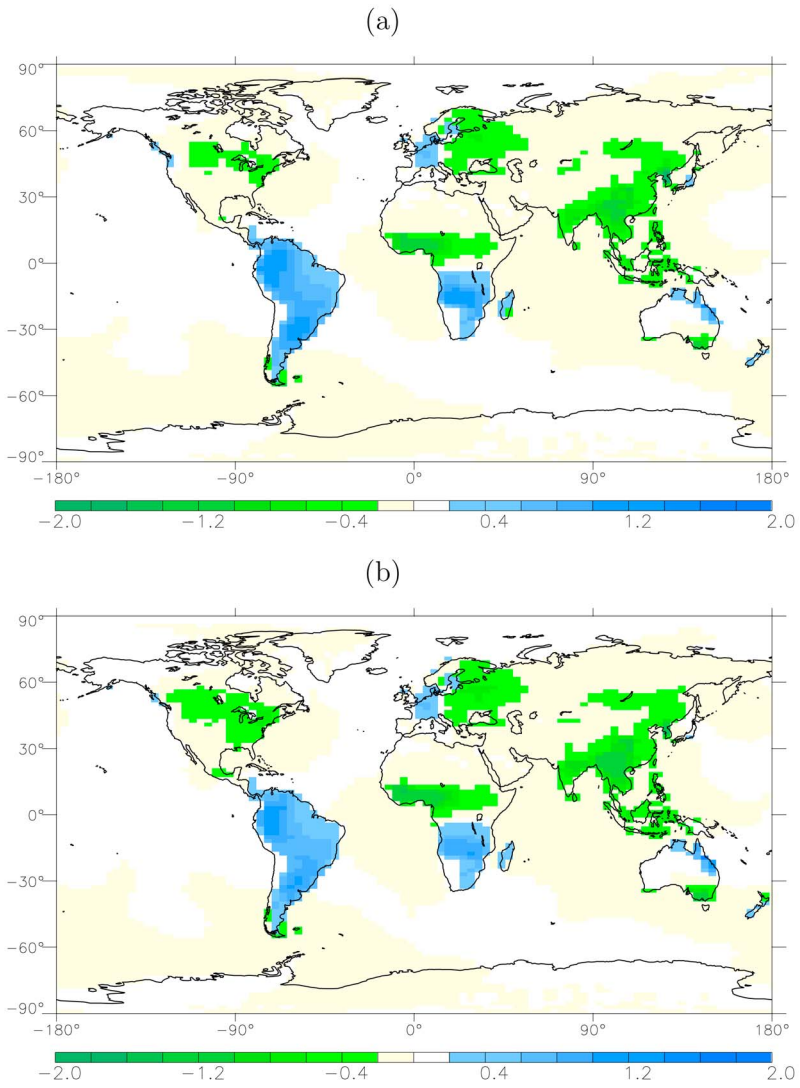

Figure 7. Flux increments (posterior minus prior fluxes) for the (a) first and (b) second weeks of 2000 (gC m^{-2} per day).

[30] The present study shows a global inversion of CO_2 fluxes over a 21 year period at a rather high resolution (3.75° × 2.5° longitude-latitude and 8 days) based on a series of routine mixing ratio measurements that are freely available from three large data sets (NOAA ESRL, CarboEurope, and WDCGG). The variational formulation of our inversion system allowed the whole period to be processed at once, which reinforced the consistency of our inversion compared to sequential approaches. The uncertainty of the inverted fluxes is rigorously estimated from the theory at various space and time scales. This quantity is particularly important for properly exploiting the inverted fluxes given its still-large values. The self-consistency of a Bayesian inversion system can be evaluated by comparing the statistics of the inversion flux increments, of the prior-minus-observation departures, and of the posterior-minus-observation departures with what the system assumes [e.g., *Desroziers et al.*, 2005]. However, following the usual practice, our prior terrestrial vegetation fluxes are annually balanced, so that the prior atmospheric simulation diverges from the observations over time and the error statistics deviate from Gaussianity. We have found such diagnostics (not shown) to be of no help in our case. We therefore evaluate the quality of the inverted fluxes with two large databases of aircraft measurements of mixing ratios (GEOMON and CONTRAIL). The "poor man's inversion" based on the observed global atmospheric growth rate provides a baseline for the evaluation and measures the inversion skill.

[31] Technically, our inversion system lies in the continuity of a series of previous studies that have attempted to infer global fluxes at the horizontal resolution of their transport models [e.g., *Kaminski et al.*, 1999; *Rödenbeck et al.*, 2003]. Some improvement is expected from the even higher resolution of the present study both for the prior error statistics, with an e-folding length as low as 500 km over land, and for the transport model. Increased resolution is motivated by the lack of spatial coherence of prior flux errors over land [*Chevallier et al.*, 2006]. This inversion also differs by many details of the implementation of the Bayesian framework, concerning the transport model, the prior fluxes, the prior

errors, the observation errors, the observation selection, and the preprocessing (if any) of the observations. It also uses a much enhanced set of sites than the earlier works, which should further pin down the flux variability in space and time.

[32] The computation of the uncertainty of the posterior (or inverted) fluxes suggests a modest improvement compared to the prior fluxes, with some remaining ambiguity between the carbon budgets of regions within the same continent. The independent observations indicate that the posterior atmospheric simulation is better than the baseline by about 1 ppm in the free troposphere, which is remarkable because many transport models produce incorrect vertical gradients [*Stephens et al.*, 2007], and thus the validation suffers from systematic transport errors. This improvement is obtained by large modifications of the interannual regional carbon budgets compared to the prior fluxes and by a change in the seasonal cycle of fluxes over land. Changes from the prior over the ocean basins are much less than the flux uncertainty. The modest improvement that we can demonstrate actually does not express the full information content of the surface network. The current generation of global transport models suffers from large uncertainties that reduce the available information content to a large extent. Indeed the modeling and representativeness errors still exceed the measurement errors by an order of magnitude. Further, some measurements are excluded, like those made at night in low-altitude stations, when the boundary layer is stable. Most of the measurements collected so far actually represent an investment for future reanalyses of the carbon budget after significant improvements of the models have been made (which may, in turn, make the inversion systems more sensitive to the differences in measurement practices between laboratories). In the meantime, the current inversion provides a reliable estimate of the carbon budget up to its estimated uncertainty.

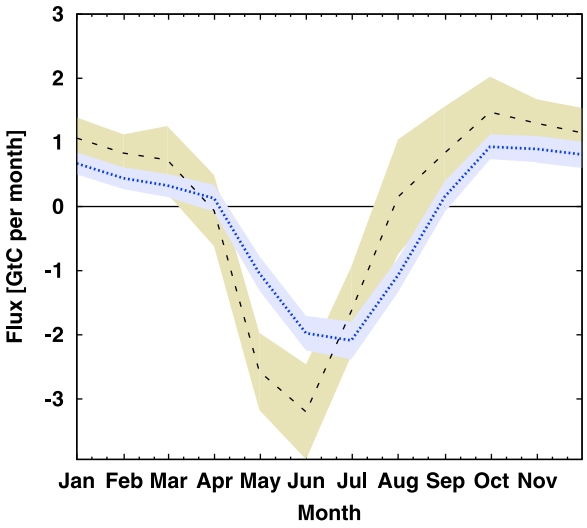

Figure 8. The 21-year-mean seasonal cycle of the prior and the posterior fluxes over the terrestrial lands north of 20°N for the period 1988–2008. The fossil fuel component given by the prior fluxes has been removed from both the prior and the posterior fluxes. In the sign convention, positive fluxes correspond to a net carbon source into the atmosphere. The black dashed line corresponds to prior fluxes, while the posterior flux time series is represented by the blue dotted line. Shaded areas show the spread of the monthly flux uncertainty, as 1 standard deviation around the prior fluxes (beige) and around the posterior fluxes (overlaid in violet). Prior and posterior standard deviations are from the ensemble used for Figure 3.

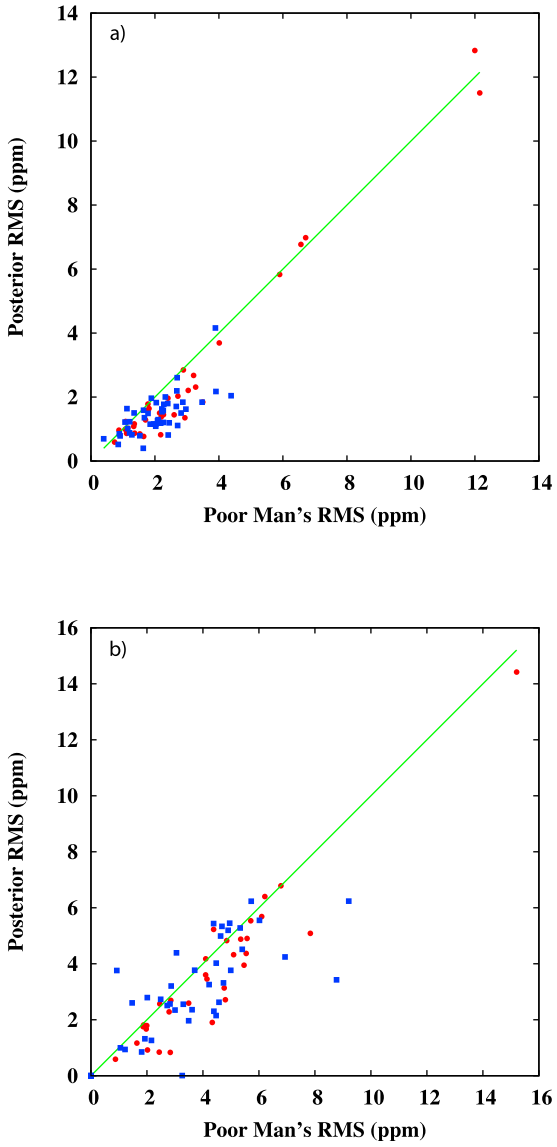

Figure 9. RMS difference between the LMDZ simulations and the pointwise aircraft measurements over the 21 year period for (a) free tropospheric (300–850 hPa) CO_2 mixing ratios and (b) boundary layer mixing ratios (990–850 hPa). LMDZ simulations use posterior fluxes or poor man's fluxes as boundary conditions. A red circle represents 1 of the 34 measurement campaigns listed in Table 3, and blue square corresponds to one airport in the CONTRAIL data set. The inversion performs better than the poor man's method at a given station when the corresponding symbol is located under the bisector (green line).

[33] **Acknowledgments.** This work was performed using HPC resources from GENCI- (CCRT/CINES/IDRIS; grant 2009- t2009012201).

It was cofunded by the European Commission under the EU Seventh Research Framework Programme (grant agreements 212196, COCOS, and 218793, MACC). The authors are very grateful to the many people involved in the surface and aircraft measurement and in the archiving of these data. All PIs have been contacted and were offered coauthorship. The authors also acknowledge the fruitful discussions with Peter Rayner and François-Marie Bréon (LSCE) about many aspects related to this study and the constructive comments made by three anonymous reviewers.

References

Berrisford, P., D. Dee, K. Fielding, M. Fuentes, P. Kallberg, S. Kobayashi, and S. Uppala (2009), *The ERA-Interim archive, ERA Rep. Ser. 1*, 16 pp., Eur. Cent. for Medium-Range Weather Forecasting, Reading, U. K.

Bousquet, P., P. Peylin, P. Ciais, C. Le Quéré, P. Friedlingstein, and P. Tans (2000), Regional changes in carbon dioxide fluxes of land and oceans since 1980, *Science*, *290*, 1342–1346, doi:10.1126/science.290.5495.1342.

Bousquet, P., et al. (2006), Contribution of atmospheric and natural sources to atmospheric methane variability, *Nature*, *443*, 439–443, doi:10.1038/nature05132.

Carouge, C., P. Peylin, P. J. Rayner, P. Bousquet, F. Chevallier, and P. Ciais (2008), What can we learn from European continuous atmospheric CO_2 measurements to quantify regional fluxes—Part 2: Sensitivity of flux accuracy to inverse setup, *Atmos. Chem. Phys. Discuss.*, *8*, 18,621–18,649, doi:10.5194/acpd-8-18621-2008.

Chevallier, F., M. Fisher, P. Peylin, S. Serrar, P. Bousquet, F.-M. Bréon, A. Chédin, and P. Ciais (2005), Inferring CO_2 sources and sinks from satellite observations: Method and application to TOVS data, *J. Geophys. Res.*, *110*, D24309, doi:10.1029/2005JD006390.

Chevallier, F., N. Viovy, M. Reichstein, and P. Ciais (2006), On the assignment of prior errors in Bayesian inversions of CO_2 surface fluxes, *Geophys. Res. Lett.*, *33*, L13802, doi:10.1029/2006GL026496.

Chevallier, F., F.-M. Bréon, and P. J. Rayner (2007), The contribution of the Orbiting Carbon Observatory to the estimation of CO_2 sources and sinks: Theoretical study in a variational data assimilation framework, *J. Geophys. Res.*, *112*, D09307, doi:10.1029/2006JD007375.

Chevallier, F., R. J. Engelen, C. Carouge, T. J. Conway, P. Peylin, C. Pickett-Heaps, M. Ramonet, P. J. Rayner, and I. Xueref-Remy (2009), AIRS-based versus surface-based estimation of carbon surface fluxes, *J. Geophys. Res.*, *114*, D20303, doi:10.1029/2009JD012311.

Courtier, P., J.-N. Thépaut, and A. Hollingworth (1994), A strategy for operational implementation of 4D-Var, using an incremental approach, *Q. J. R. Meteorol. Soc.*, *120*, 1367–1387, doi:10.1002/qj.49712051912.

Denman, K. L., et al. (2007), Couplings between changes in the climate system and biogeochemistry, in *Climate Change 2007: The Physical Science Basis. Contribution of Working Group I to the Fourth Assessment Report of the Intergovernmental Panel on Climate Change*, edited by S. Solomon et al., pp. 499–587, Cambridge Univ. Press, Cambridge, U. K.

Desroziers, G., L. Berre, B. Chapnik, and P. Poli (2005), Diagnosis of observation, background and analysis error statistics in observation space, *Q. J. R. Meteorol. Soc.*, *131*, 3385–3396, doi:10.1256/qj.05.108.

Fisher, M., and P. Courtier (1995), *Estimating the covariance matrices of analysis and forecast error in variational data assimilation, Tech. Mem. 220*, 26 pp., Eur. Cent. for Medium-Range Weather Forecasting, Reading, U. K.

GLOBALVIEW-CO (2008), Cooperative Atmospheric Data Integration Project—Carbon Monoxide [CD-ROM], *Earth Syst. Res. Lab.*, Natl. Ocean. Atmos. Admin., Boulder, Colo. (Available at ftp://ftp.cmdl.noaa.gov/ccg/co/GLOBALVIEW)

GLOBALVIEW-CO2 (2009), Cooperative Atmospheric Data Integration Project—Carbon Dioxide [CD-ROM], *Earth Syst. Res. Lab.*, Natl. Ocean. Atmos. Admin., Boulder, Colo. (Available at ftp://ftp.cmdl.noaa.gov/ccg/co2/GLOBALVIEW)

Gurney, K. R., et al. (2002), Towards robust regional estimates of CO_2 sources and sinks using atmospheric transport models, *Nature*, *415*(6872), 626–630, doi:10.1038/415626a.

Hourdin, F., et al. (2006), The LMDZ4 general circulation model: Climate performance and sensitivity to parametrized physics with emphasis on tropical convection, *Clim. Dyn.*, *27*, 787–813, doi:10.1007/s00382-006-0158-0.

Kaminski, T., M. Heimann, and R. Giering (1999), A coarse grid three-dimensional global inverse model of the atmospheric transport: 2. Inversion of the transport of CO_2 in the 1980s, *J. Geophys. Res.*, *104*, 18,555–18,581, doi:10.1029/1999JD900146.

Krinner, G., N. Viovy, N. de Noblet-Ducoudré, J. Ogée, J. Polcher, P. Friedlingstein, P. Ciais, S. Sitch, and I. C. Prentice (2005), A dynamic global vegetation model for studies of the coupled atmosphere-biosphere system, *Global Biogeochem. Cycles*, *19*, GB1015, doi:10.1029/2003GB002199.

Lauvaux, T., et al. (2009a), Bridging the gap between atmospheric concentrations and local ecosystem measurements, *Geophys. Res. Lett.*, *36*, L19809, doi:10.1029/2009GL039574.

Lauvaux, T., O. Pannekoucke, C. Sarrat, F. Chevallier, P. Ciais, J. Noilhan, and P. J. Rayner (2009b), Structure of the transport uncertainty in mesoscale inversions of CO_2 sources and sinks using ensemble model simulations, *Biogeosciences*, *5*, 4813–4846.

Law, R. M., et al. (2008), TransCom model simulations of hourly atmospheric CO_2: Experimental overview and diurnal cycle results for 2002, *Global Biogeochem. Cycles*, *22*, GB3009, doi:10.1029/2007GB003050.

Le Quéré, C., et al. (2007), Saturation of the Southern Ocean CO_2 sink due to recent climate change, *Science*, *316*, 1735–1738, doi:10.1126/science.1136188.

Machida, T., et al. (2008), Worldwide measurements of atmospheric CO_2 and other trace gas species using commercial airlines, *J. Atmos. Oceanic Technol.*, *25*(10), 1744–1754, doi:10.1175/2008JTECHA1082.1.

Masarie, K. A., and P. P. Tans (1995), Extension and integration of atmospheric carbon dioxide data into a globally consistent measurement record, *J. Geophys. Res.*, *100*(D6), 11,593–11,610, doi:10.1029/95JD00859.

Olivier, J. G. J., and J. J. M. Berdowski (2001), Global emissions sources and sinks, in *The Climate System*, edited by J. Berdowski, R. Guicherit, and B. J. Heij, pp. 33–78, A. A. Balkema, Lisse, Netherlands.

Patra, P. K., et al. (2008), TransCom model simulations of hourly atmospheric CO_2: Analysis of synoptic-scale variations for the period 2002–2003, *Global Biogeochem. Cycles*, *22*, GB4013, doi:10.1029/2007GB003081.

Peters, W., et al. (2007), An atmospheric perspective on North American carbon dioxide exchange: CarbonTracker, *Proc. Natl. Acad. Sci. U. S. A.*, *104*, 18,925–18,930, doi:10.1073/pnas.0708986104.

Peylin, P., F. M. Bréon, S. Serrar, Y. Tiwari, A. Chédin, M. Gloor, T. Machida, C. Brenninkmeijer, A. Zahn, and P. Ciais (2007), Evaluation of Television Infrared Observation Satellite (TIROS-N) Operational Vertical Sounder (TOVS) spaceborne CO_2 estimates using model simulations and aircraft data, *J. Geophys. Res.*, *112*, D09313, doi:10.1029/2005JD007018.

Randerson, J. T., G. R. van der Werf, L. Giglio, G. J. Collatz, and P. S. Kasibhatla (2007), Global Fire Emissions Database, version 2.1, Oak Ridge Natl. Lab., Oak Ridge, Tenn., doi:10.3334/ORNLDAAC/849.

Rödenbeck, C., S. Houweling, M. Gloor, and M. Heimann (2003), CO_2 flux history 1982–2001 inferred from atmospheric data using a global inversion of atmospheric transport, *Atmos. Chem. Phys.*, *3*, 1919–1964, doi:10.5194/acp-3-1919-2003.

Rödenbeck, C., T. J. Conway, and R. L. Langenfelds (2006), The effect of systematic measurement errors on atmospheric CO_2 inversions: A quantitative assessment, *Atmos. Chem. Phys.*, *6*, 149–161, doi:10.5194/acp-6-149-2006.

Stephens, B. B., et al. (2007), Weak northern and strong tropical land carbon uptake from vertical profiles of atmospheric CO_2, *Science*, *316*, 1732–1735, doi:10.1126/science.1137004.

Takahashi, T., S. C. Sutherland, and A. Kozyr (2007), Global Ocean Surface Water Partial Pressure of CO_2 Database: Measurements performed during 1968–2007, version 2007, *ORNL/CDIAC-152, NDP-088a*, 20 pp., Carbon Dioxide Inf. Anal. Cent., Oak Ridge Natl. Lab., U.S. Dep. of Energy, Oak Ridge, Tenn.

Takahashi, T., et al. (2009), Climatological mean and decadal change in surface ocean pCO_2, and net sea-air CO_2 flux over the global oceans, *Deep Sea Res., Part II*, *56*, 554–577, doi:10.1016/j.dsr2.2008.12.009.

van der Werf, G. R., J. T. Randerson, G. J. Collatz, L. Giglio, P. S. Kasibhatla, A. F. Arellano, S. C. Olsen, and E. S. Kasischke (2004), Continental-scale partitioning of fire emissions during the 1997 to 2001 El Niño/La Niña period, *Science*, *303*(5654), 73–76, doi:10.1126/science.1090753.

T. Aalto, Finnish Meteorological Institute, Erik Palmenin Aukio 1, PO Box 503, FI-00101 Helsinki, Finland.

B. E. Anderson and S. A. Vay, Langley Research Center, NASA, Hampton, VA 23681, USA.

P. Bousquet, F. Chevallier, P. Ciais, F. Maignan, P. Peylin, M. Ramonet, L. Rivier, and M. Schmidt, Laboratoire des Sciences du Climat et de l'Environnement, CEA-CNRS-UVSQ, IPSL, L' Orme des Merisiers, Bât. 701, F-91191 Gif-sur-Yvette, France. (frederic.chevallier@lsce.ipsl.fr)

E. G. Brunke, South African Weather Service, PO Box 320, Stellenbosch, 7599 South Africa.

L. Ciattaglia, ICES CNR-IDAC, Via del Fosso del Cavaliere 100, I-00133 Rome, Italy.

T. J. Conway, Earth System Research Laboratory, NOAA, 325 Broadway, Boulder, CO 80305-3328, USA.

Y. Esaki, Japan Meteorological Agency, 1-3-4 Otemachi, Chiyoda-ku, Tokyo 100-8122, Japan.

M. Fröhlich, Umweltbundesamt GmbH, Spittelauer Lände 5, A-1090 Vienna, Austria.

A. Gomez, National Institute for Water and Atmospheric Research, 301 Evans Bay Parade, Wellington 6021, New Zealand.

A. J. Gomez-Pelaez, Meteorological State Agency of Spain, E-38071 Santa Cruz de Tenerife, Spain.

L. Haszpra, Hungarian Meteorological Service, PO Box 39, H-1675 Budapest, Hungary.

P. Krummel, R. Langenfelds, and P. Steele, CSIRO Marine and Atmospheric Research, 107-121 Station Street, Aspendale, Vic 3195, Australia.

M. Leuenberger, Climate and Environmental Physics, Physics Institute, University of Bern, Sidlerstrasse 5, CH-3012 Bern, Switzerland.

T. Machida and H. Mukai, National Institute for Environmental Studies, 16-2 Onogawa, Tsukuba, 305-8506 Ibaraki, Japan.

H. Matsueda and Y. Sawa, Meteorological Research Institute, 1-1 Nagamine, Tsukuba, 305-0052 Ibaraki, Japan.

J. A. Morguí, Laboratori de Recerca del Clima, Baldiri i Reixach, 4-6, Torre D, E-08028 Barcelona, Spain.

T. Nakazawa, Tohoku University, Sendai, 981-8555 Miyagi, Japan.

A. T. Vermeulen, Energy Research Centre of the Netherlands, PO Box 1, NL-1755 ZG Petten, Netherlands.

S. Wofsy, School of Engineering and Applied Sciences, Harvard University, 29 Oxford St., Cambridge, MA 02138, USA.

D. Worthy, Environment Canada, 4905 Dufferin St., Downsview, ON M3H 5T4, Canada.